European Journal of Mechanics B/Fluids 29 (2010) 236–245

Contents lists available at ScienceDirect

European Journal of Mechanics B/Fluids

journal homepage: www.elsevier.com/locate/ejmflu

Computational studies of the pitched blade turbines design effect on the stirred tank flow characteristics

Z. Driss *, G. Bouzgarrou, W. Chtourou, H. Kchaou, M.S. Abid

National School of Engineers of Sfax (ENIS), Laboratory of Electro-Mechanic Systems (LASEM), B.P. 1173, km 3.5 Soukra, 3038 Sfax, Tunisia

ARTICLE INFO

Article history:
Received 8 July 2009
Received in revised form
11 November 2009
Accepted 29 January 2010
Available online 7 February 2010

Keywords:
CFD
Modeling
Turbulent flow
Finite volume
Meshing generation
PBT

ABSTRACT

A specific computational fluid dynamics (CFD) code is developed to predict the turbulent flow field in a stirred tank equipped with the pitched blade turbines (PBT) and to choose the most effective agitation system. The computer method permits the numerical analyses of turbines with complex geometries. After defining the list of nodes belonging to the interface separating the turbine shape and the flow domain, the meshes in the flow domain are automatically generated on a finite volume discretization. The three-dimensional flow of a fluid is numerically analyzed using the Navier–Stokes equations in conjunction with the standard k–ε turbulence model. The effects of inclined angle on the local and global flow characteristics have been particularly determined. To verify our computer simulations, the power numbers were measured and compared with computer results. Also, the flow patterns have been compared with the ones found by other experimental results. These matching results indicate the validity of our computer method.

1. Introduction

Mechanically stirred tanks are frequently used in industrial application such as foods, cosmetics, pharmaceuticals, plastics and rubbers. For the rational design of such equipments some of the following transport characteristics are usually used in the design of the equipment. A detailed knowledge of velocity, power and mixing characteristics of stirred tank configurations is therefore required. The optimum design of a stirred tank depends on the desired production rate with specified product properties and is achieved by the correct choice of tank and impeller geometry, rotational speed and location of fluid addition and subtraction. Direct experience can be used to select the best kind of equipment, predicting how well and quickly it will perform and what power consumption will be [1]. Generally, this method is very expensive because the construction of test bench asks for the respect of the real ladders of the studied phenomenon. Also, it requires an effective material and a very precise instrumentation. In addition, due to the hazards linked to thermal runaways, laboratory and pilot-plant scale experiments in runaway conditions are difficult to carry out. Therefore, the use of a computer method is extremely important for simulating the behavior of systems involving fluid flow, heat transfer and other related physical processes [2,3]. Nowadays, the considerable advances made in computing efficiency, coupled with the development of advanced solvers and algorithms which enable robust solution of the flow field, have made computational fluid dynamics (CFD) an efficient and powerful tool for both industrial and research purposes. Particularly, modeling a stirred tank using CFD is covered in many papers. For example, the main aims of Aubin et al. [4] are to characterize the single phase turbulent flow in a tank stirred by a 45° PBT using CFD. The effect of the modeling approach, discretization scheme and turbulence model on mean velocities, turbulent kinetic energy and global quantities, such as the power and circulation numbers, has been investigated. The stationary and time-dependent modeling approaches were found to have little effect on the turbulent flow, however the choice of the numerical scheme was found to be important, especially for the predicted turbulent kinetic energy. Hollander et al. [5] presented a numerical study on the scale-up behavior of orthokinetic agglomeration in stirred tanks. Large Eddy flow simulations were performed to obtain an accurate description of the turbulent flow encountered in stirred vessels, equipped with either a Rushton turbine or a 45° PBT. It was found that impeller shape, vessel size and Reynolds number have a profound effect on reactor performance. Dakshinamoorthy et al. [6] studied shortstopping results in vessels agitated with jets and impellers using the commercial CFD code Fluent. The simulated shortstopping results with the jet mixer are then compared with those obtained with Rushton turbine and 45° PBT. These results identify the conditions for effective shortstopping. The distribution of excess inhibitor is shown to be an important and essential design criterion for effective shortstopping when using impeller stirred vessels. Kumaresan and Joshi [7] presented the comparison

* Corresponding author. Tel.: +216 74 274 088; fax: +216 74 275 595.
E-mail addresses: Zied.Driss@enis.rnu.tn, Zied_Driss@yahoo.fr (Z. Driss).

0997-7546/$ – see front matter
doi:10.1016/j.euromechflu.2010.01.006

Nomenclature

A	Van-Driest constant
$C_{1\varepsilon}$	constant in the standard k–ε model
$C_{2\varepsilon}$	constant in the standard k–ε model
C_μ	constant in the standard k–ε model
d	turbine diameter, m
D	internal diameter of the vessel tank, m
Fr	Froude number, dimensionless, $Fr = \frac{(2\pi N)^2 d}{g}$
G	turbulent kinetic energy production, dimensionless
g	gravity acceleration, m^2 s^{-1}
h	turbine position, m
H	vessel tank height, m
I	computational cell in radial direction, dimensionless
J	computational cell in tangential direction, dimensionless
K	computational cell in axial direction, dimensionless
k	turbulent kinetic energy, dimensionless
l_m	mixing length, dimensionless
N	velocity of the turbine, rad s^{-1}
N_p	power number, dimensionless, $N_p = \frac{P}{\rho N^3 d^5}$
NR	radial nodes number, dimensionless
NZ	axial nodes number, dimensionless
P	power, W
p	pressure, dimensionless
Re	Reynolds number, dimensionless, $Re = \frac{\rho N d^2}{\mu}$
r	radial coordinate, dimensionless
S_Φ	sink term, dimensionless
s	shaft diameter, m
t	time, s
U	radial velocity components, dimensionless
V	angular velocity components, dimensionless
V_0	rubbing velocity on the wall, m s^{-1}
V_R	velocity neighbour to the wall, dimensionless
W	axial velocity components, dimensionless
y	distance of the adjacent node to the solid wall, m
y^+	local Reynolds number, dimensionless
z	axial coordinate, dimensionless
$\overrightarrow{V}$	velocity vector
$\overrightarrow{J}_\Phi$	flux term vector
$\overline{\overline{I}}$	identity tensor

Greek symbols

β	inclined angle, degrees
ε	dissipation rate of the turbulent kinetic energy, dimensionless
θ	angular coordinate, rad
κ	Von Karman constant
μ	fluid viscosity, Pas
υ_e	effective viscosity, dimensionless
υ_t	turbulent viscosity, dimensionless
ρ	fluid density, kg m^{-3}
σ_k	constant in the standard k–ε model
σ_ε	constant in the standard k–ε model
Γ_Φ	diffusion coefficient, dimensionless
ΔR	radial length between two nodes, dimensionless
ΔZ	axial length between two nodes, dimensionless
Φ	general transport parameter, dimensionless
Φ_v	viscous dissipation rate, dimensionless
$\overline{\overline{\tau}}$	stress tensor
$\overline{\overline{\tau}}_R$	Reynolds tensor

Abbreviations

CFD	computational fluid dynamics
CAD	computer aided design
CSD	computational structure dynamics
PBT	pitched blade turbine
LDA	Laser doppler anemometry
l	laminar
t	turbulent

of the flow pattern on the basis of equal power consumption to characterize the flow generated by different impeller geometries. Comparisons of laser doppler anemometry (LDA) measurements and CFD predictions have been presented. The good comparison indicates the validity of the CFD model. Deglon and Meyer [8] demonstrated that the multiple reference frames impeller rotation model and the standard k–ε turbulence model, as commonly used in engineering CFD simulations of stirred tanks, can accurately model turbulent fluid flow. In this study, the CFD software Fluent 6 is used to simulate flow in a small tank. Simulations are conducted on four grids of significantly different resolution using the upwind, central and Quick discretization schemes. CFD model results are evaluated in terms of the predicted flow field, power number, mean velocity components and turbulent kinetic energy using published experimental data. Armenante et al. [9] presented the velocity profiles and the turbulent kinetic energy distribution of a flow generated by a 6-blade, 45° PBT in an unbaffled, flat-bottom, cylindrical tank provided with a lid, and completely filled with water. The mean and fluctuating velocities in all three directions were experimentally measured with a laser doppler velocimeter (LDV) at five different heights and twenty radial positions within the vessel.

On the basis of the previous studies, we can confirm that the 45° PBT is frequently used in many applications. As a consequence, it appears important to study different configurations and to make a comparison between them through a CFD simulation. For this purpose, a computer method has been developed to study the pitched blade turbines design effect on the stirred tank flow characteristics. The present work aims the characterization of the local and global hydrodynamics of three types of PBT configurations defined by the inclined angles β equals to 45°, 60° and 75°.

2. Geometry system

The system under investigation in the current paper is a stirred tank equipped with a six-blade PBT. The tank is a vertical cylindrical vessel with a height-to-diameter ratio H/D of 1. The shaft is placed concentrically with a diameter ratio s/D of 0.04. The tip to tip turbine diameter ratio d/D is a 0.33 and the turbine position ratio y/D is a 0.25. Three inclined angles β equals to 45°, 60° and 75° were considered (Fig. 1). The first geometry system is similar to Armenante application system [9].

3. Computer method

3.1. Governing equations

This model is characterized by the solution of an individual set of continuity and momentum equations [10]. The continuity equation is a statement of conservation of mass given in the following form:

$$div\,\overrightarrow{V} = 0. \tag{1}$$

The momentum equation is a statement of conservation of momentum in each of the three component directions. The three momentum equations are collectively called the Navier–Stokes

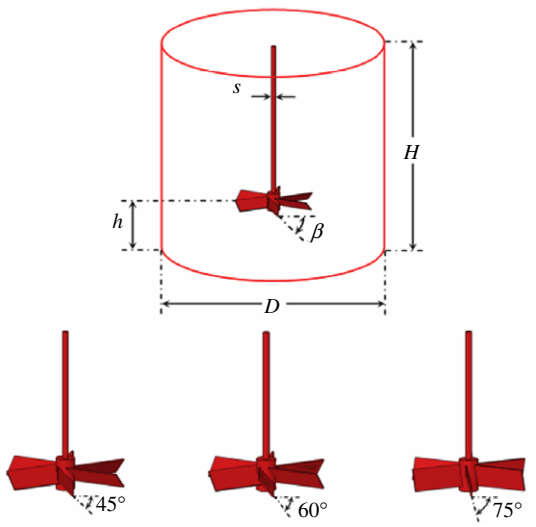

(a) PBT 45°. (b) PBT 60°. (c) PBT 75°.

Fig. 1. A stirred tank equipped with pitched blade turbines.

equations. They are written in a rotating frame reference. Therefore, the centrifugal and the Coriolis accelerations terms are added to the momentum equations given in the following form:

$$\frac{\partial(\rho\overrightarrow{V})}{\partial t} + div(\rho\overrightarrow{V}\otimes\overrightarrow{V} + p\bar{\bar{I}}) = div(\bar{\bar{\tau}} + \bar{\bar{\tau}}_R) + \rho\left(N^2\overrightarrow{r} - 2\overrightarrow{N}\wedge\overrightarrow{V}\right). \quad (2)$$

The non linearity aspect is done through the use of a turbulence problem. In fact, several methods are available for including turbulence in the Navier–Stokes equations. Most of these involve a process of time-averaging the conservation equations. When turbulence is included, the transported quantity is assumed to be the sum of an equilibrium and a fluctuating component. The only term that remains positive definite is one containing the product of two fluctuating terms. The new terms involving are called the Reynolds stresses. Reynolds stresses contribute new unknowns to the equations, and need to be related to the other variables. The Boussinesq hypothesis makes the assumption that the Reynolds stresses can be expressed in terms of mean velocity gradients. The statement of the hypothesis below, shows the introduction of a new constant that is dimensionally equivalent to viscosity. The new constant is the turbulent viscosity υ_t. The hypothesis also introduces another term involving a new variable k, the turbulent kinetic energy. The turbulent viscosity υ_t is derived from both k and ε, and involves a constant taken from experimental data. The above models retain the turbulent viscosity form of the standard k–ε and thus cannot predict effect depending on the nonlinearity of the stress–strain relationship. To summarize the solution process for the k–ε model, transport equations are solved for the turbulent kinetic energy k and the dissipation rate of the turbulent kinetic energy ε. The solutions for k and ε are used to compute the turbulent viscosity υ_t. Using these results, the Reynolds stresses can be computed for substitution into the momentum equations. Once the momentum equations have been solved, the new velocity components are used to update the turbulence generation term and the process is repeated. The k–ε model is one of a family of two-equation models, for which two additional transport equations must be solved in order to compute the Reynolds stresses. This model is robust and economical. Its main advantages are a rapid, stable calculation and reasonable results for many flows [11]. It is semi-empirical, based in large part on observations of mostly high Reynolds number flows. The two transport equations that need to be solved for this model are for the kinetic energy of turbulence k and the rate of dissipation of turbulence ε [10]. The standard k–ε turbulence equations are given in the following form:

$$\frac{\partial k}{\partial t} + div\left[\overrightarrow{V}k - \frac{2}{\pi}\left(\frac{d}{D}\right)^2\frac{1}{Re}\left(1+\frac{\upsilon_t}{\sigma_k}\right)\overrightarrow{grad}\,k\right] = \frac{2}{\pi}\left(\frac{d}{D}\right)^2\frac{1}{Re}G - \varepsilon \quad (3)$$

$$\frac{\partial \varepsilon}{\partial t} + div\left[\overrightarrow{V}\varepsilon - \frac{2}{\pi}\left(\frac{d}{D}\right)^2\frac{1}{Re}\left(1+\frac{\upsilon_t}{\sigma_\varepsilon}\right)\overrightarrow{grad}\,\varepsilon\right] = \frac{\varepsilon}{k}\left[C_{1\varepsilon}\frac{2}{\pi}\left(\frac{d}{D}\right)^2\frac{1}{Re}G - C_{2\varepsilon}\varepsilon\right]. \quad (4)$$

The turbulent kinetic energy production is given in the following form:

$$G = \upsilon_t\left[2\left[\left(\frac{\partial U}{\partial r}\right)^2 + \left(\frac{\partial V}{r\partial\theta} + \frac{U}{r}\right)^2 + \left(\frac{\partial W}{\partial z}\right)^2\right] + \left[\frac{\partial V}{\partial r} - \frac{V}{r} + \frac{\partial U}{r\partial\theta}\right]^2 + \left[\frac{\partial W}{r\partial\theta} + \frac{\partial V}{\partial z}\right]^2 + \left[\frac{\partial U}{\partial z} + \frac{\partial W}{\partial r}\right]^2\right]. \quad (5)$$

The viscosity equations [12] are given in the following form:

$$\upsilon_t = C_\mu\frac{\pi}{2}\left(\frac{D}{d}\right)^2 Re\frac{k^2}{\varepsilon} \quad (6)$$

$$\upsilon_e = 1 + \upsilon_t. \quad (7)$$

The Reynolds number [12] is given in the following form:

$$Re = \frac{\rho N d^2}{\mu}. \quad (8)$$

The constants of the standard k–ε model were presented in Table 1.

Table 1
Standard k–ε model constants.

$C_{1\varepsilon}$	$C_{2\varepsilon}$	C_μ	σ_k	σ_ε
1.44	1.92	0.09	1	1.3

3.2. CFD code presentation

Modeling a stirred tank using CFD requires consideration of many aspects of the process. The motion of the impeller in the tank must be treated in a special way. The special treatment employed impacts both the construction of the computational grid as well as the solution method used to numerically obtain the flow field. The basic principle is to split the domain under investigation into small elements. For each one of these elements, a set of partial differential equations is solved, which approximates a solution for the flow in order to achieve the conditions of conservation of mass and momentum. The basic equations are solved simultaneously with any additional equations implemented in a particular model to obtain the flow patterns, pressure, characteristics of turbulence and any derived quantities [13]. For easy access, our specific CFD code contains three main elements: pre-processor, processor and post-processor (Fig. 2).

3.2.1. Pre-processor

The pre-processor serves as a source of input for the CFD code by means of an operator interface. This is transformed into a suitable form for the processor. The user activities at the pre-processing

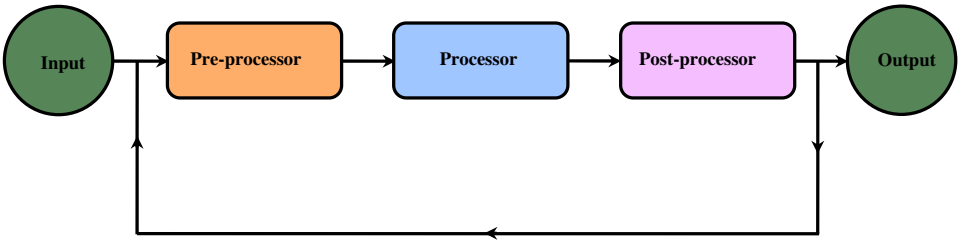

Fig. 2. Schematic presentation of CFD code.

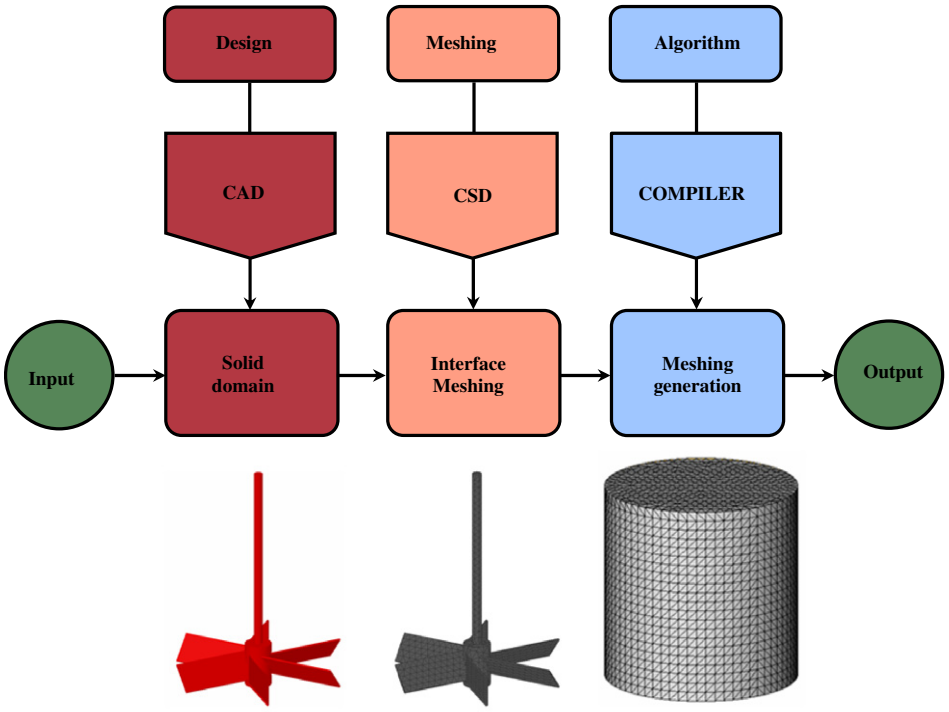

Fig. 3. Schematic presentation of the pre-processor.

stage involve definition of the geometry, mesh generation and specification of the appropriate boundary conditions. The computational model requires that the volume occupied by the fluid inside the vessel to be described by a computational grid or cells. In these cells, variables are computed and stored. The computational grid must fit the contours of the vessel and its internals, even if the components are geometrically complex. For this reason, the computer aided design (CAD) is used at first to construct the turbine shape. After that, a list of nodes is defined to belong to the interface separating the solid domain from the fluid domain passing through the computational structure dynamics (CSD) code. Using this list, the mesh in the flow domain is automatically generated for the three-dimensional simulations (Fig. 3). The computational mesh for our system geometry contained 54 000 nodes. A staggered mesh is used in such a way that four different control volumes are defined for a given node point, one for each of the three vector components and one for the scalar variable (Fig. 4). Therefore, the region to be modeled is subdivided into a number of control volumes defined on a cylindrical coordinates system [14].

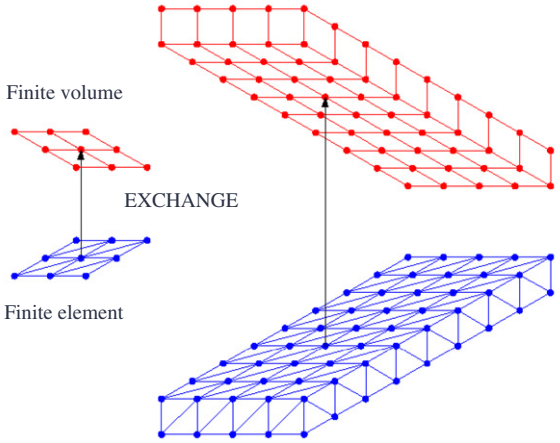

Fig. 4. Node points of a staggered mesh.

3.2.2. Processor

Solutions of the Navier–Stokes equations in conjunction with the standard k–ε turbulence model are developed using a control volume discretization method. Numerical methods consist on an approximation of the unknown flow variables by means of simple functions and a discretization by substitution of the approximation into the governing flow equations and subsequent mathematical manipulations. The finite volume method consists on the formal integration of the governing equations of fluid flow over all the control volumes of the solution domain. The transport equations are integrated over its own control volume using the hybrid scheme discretization method. The pressure–velocity coupling is

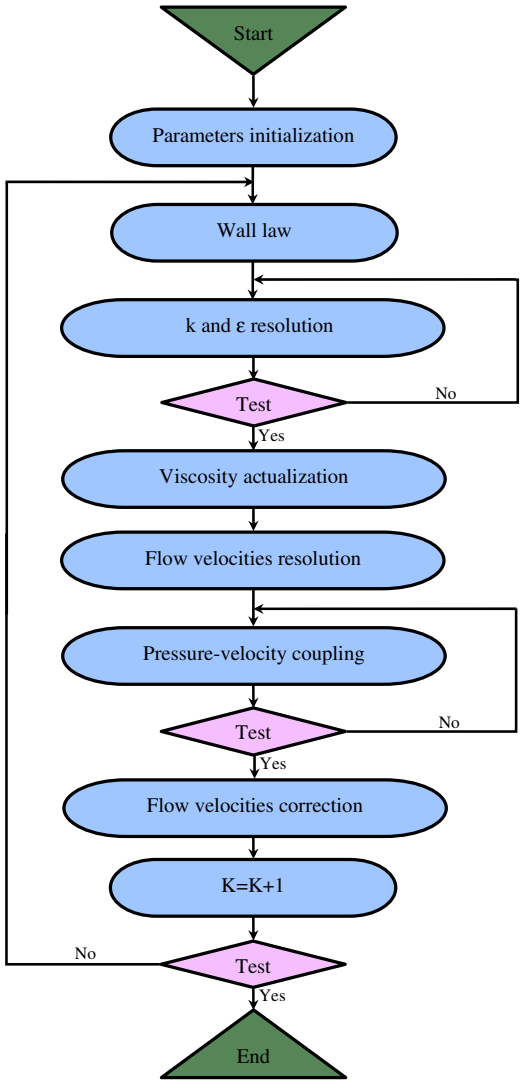

Fig. 5. Numerical algorithm.

handled by the SIMPLE algorithm of Patankar [15]. The algebraic equations solutions are obtained in reference to the fundamental paper published by Douglas and Gunn [16]. The control volume integration, distinguishes the finite volume method from all other computers techniques. The resulting statements express the conservation of relevant properties for each finite size cell. This clear relationship between the numerical algorithm and the underlying physical conservation principle forms one of the main attractions of the finite volume method and makes its concepts much simpler to understand by engineers than the finite element (Fig. 5). The conservation of a general flow variable within a finite control volume can be expressed as a balance between the various processes tending to increase or decrease it. The appropriate equations in the range of turbulent flow for an incompressible Newtonian fluid are expressed in the general conservation form [10] which can be written as follows:

$$\frac{\partial}{\partial t}\iiint_D \Phi \mathrm{d}v = -\iiint_D div\vec{J}_\Phi \mathrm{d}v + \iiint_D S_\Phi \mathrm{d}v. \tag{9}$$

With:

$$\overrightarrow{J}_\Phi = \Phi\,\overrightarrow{V} - \Gamma_\Phi \overrightarrow{grad}\,\Phi. \tag{10}$$

Using vector notation and cylindrical coordinates (r, θ, z), which of course are the most natural choice for cylindrical stirred vessels, the definition of Φ, $\overrightarrow{J}_\Phi$ and S_Φ for each equation is given, in dimensionless form, in Table 2. The discretization techniques are suitable for the treatment of the key transport phenomena, convection and diffusion as well as for the source terms and the rate of change with respect to time. The underlying physical phenomena are complex and non-linear so an iterative solution approach is required. The solution to the flow problem is defined at nodes inside each cell. Both the accuracy of the solution and its costs in terms of necessary computer hardware and calculation time are dependent on the fitness of the grid. The residuals for both velocity and pressure during the solution process were required to converge below 10^{-6}.

3.2.3. Post-processor

A huge resource has been devoted to the development post-processing techniques and display. Owing to the increased popularity of engineering workstations, many of which have outstanding graphics capabilities. These include geometry domain, grid display, vector plots, surface plots and view manipulation. Several results can be gotten such as the velocity field, the viscous dissipation rate, the characteristics of turbulence and the power number. Also, it's possible to exchange data through the post-processor with other codes or other interfaces [16].

3.3. Boundary conditions

The rotation of the turbine induced a periodic flow in a fixed reference frame. To obtain a steady state mode and to simplify the writing of the boundary conditions, a rotating reference frame fixed on the turbine shaft has been chosen. It is similar to a fixed impeller and a rotating tank which turns at the same rotating velocity but in opposed direction, by taking into account the centrifugal and Coriolis accelerations [14].

3.3.1. Velocity components

On all rigid walls, a setting no-slip condition has been prescribed. Thus, in order to take into account the presence of the turbine, all velocity components mesh nodes, which intersected with turbine, were taken equal to zero.

$$U(I, J, K) = 0 \tag{11}$$

$$V(I, J, K) = 0 \tag{12}$$

$$W(I, J, K) = 0. \tag{13}$$

At the internal wall tank, the angular velocity component has been set equal to the rotating speed because of the rotating frame reference. Therefore, in dimensionless variables:

$$V(NR - 1, J, K) = -1. \tag{14}$$

Otherwise, all radial as well as axial velocity mesh nodes were taken equal to zero:

$$U(NR - 1, J, K) = 0 \tag{15}$$

$$W(NR - 1, J, K) = 0. \tag{16}$$

In the closed tank, the surface of the liquid is always considered as plane that is to say that the vortex phenomenon is considered to be absent. This is warranted because Coriolis forces are reduced due to a decrease of the tangential motion. The liquid surface corresponds to the following conditions:

$$\frac{\partial U}{\partial z}(I, J, NZ - 1) = 0 \tag{17}$$

$$\frac{\partial V}{\partial z}(I, J, NZ - 1) = 0 \tag{18}$$

$$W(I, J, NZ - 1) = 0. \tag{19}$$

At the lateral surface of the computational domain, zero velocity gradients are assumed.

Table 2
Dimensionless form of flux and sink terms.

Φ	Flux terms $\overrightarrow{J}_{\Phi}$	Sink terms S_{Φ}
1	$\overrightarrow{V}$	0
U	$-\frac{2}{\pi}\left(\frac{d}{D}\right)^2\frac{1}{Re}\left(\upsilon_e\overrightarrow{grad}\,U\right)+\overrightarrow{V}U$	$-\frac{\partial p}{\partial r}+\frac{2}{\pi}\left(\frac{d}{D}\right)^2\frac{1}{Re}\left[-2\upsilon_e\left[\frac{U}{r^2}+\frac{1}{r^2}\frac{\partial V}{\partial\theta}\right]+\frac{1}{r}\frac{\partial}{\partial r}\left[r\upsilon_e\frac{\partial U}{\partial r}\right]+\frac{\partial}{r\partial\theta}\left[\upsilon_e r\frac{\partial}{\partial r}\left(\frac{V}{r}\right)\right]+\frac{\partial}{\partial z}\left[\upsilon_e\frac{\partial W}{\partial r}\right]\right]+\frac{V^2}{r}+r+2V$
V	$-\frac{2}{\pi}\left(\frac{d}{D}\right)^2\frac{1}{Re}\left(\upsilon_e\overrightarrow{grad}\,V\right)+\overrightarrow{V}V$	$-\frac{\partial p}{r\partial\theta}+\frac{2}{\pi}\left(\frac{d}{D}\right)^2\frac{1}{Re}\left[\upsilon_e\left[\frac{1}{r^2}\frac{\partial u}{\partial\theta}+\frac{\partial}{\partial r}\left(\frac{V}{r}\right)\right]+\frac{1}{r}\frac{\partial}{\partial r}\left[\upsilon_e\left(\frac{\partial U}{\partial\theta}-V\right)\right]+\frac{\partial}{r\partial\theta}\left[\upsilon_e\left(\frac{\partial V}{r\partial\theta}+\frac{2U}{r}\right)\right]+\frac{\partial}{\partial z}\left[\upsilon_e\frac{\partial W}{r\partial\theta}\right]\right]-\frac{UV}{r}-2U$
W	$-\frac{2}{\pi}\left(\frac{d}{D}\right)^2\frac{1}{Re}\left(\upsilon_e\overrightarrow{grad}\,W\right)+\overrightarrow{V}W$	$-\frac{\partial p}{\partial z}+\frac{2}{\pi}\left(\frac{d}{D}\right)^2\frac{1}{Re}\left[\frac{1}{r}\frac{\partial}{\partial r}\left(r\upsilon_e\frac{\partial U}{\partial z}\right)+\frac{\partial}{r\partial\theta}\left(\upsilon_e\frac{\partial V}{\partial z}\right)+\frac{\partial}{\partial z}\left(\upsilon_e\frac{\partial W}{\partial z}\right)\right]+\frac{1}{Fr}$
k	$-\frac{2}{\pi}\left(\frac{d}{D}\right)^2\frac{1}{Re}\left[\left(1+\frac{\upsilon_t}{\sigma_k}\right)\overrightarrow{grad}\,k\right]+\overrightarrow{V}k$	$\frac{2}{\pi}\left(\frac{d}{D}\right)^2\frac{1}{Re}G-\varepsilon$
ε	$-\frac{2}{\pi}\left(\frac{d}{D}\right)^2\frac{1}{Re}\left[\left(1+\frac{\upsilon_t}{\sigma_\varepsilon}\right)\overrightarrow{grad}\,\varepsilon\right]+\overrightarrow{V}\varepsilon$	$\frac{\varepsilon}{k}\left(C_{1\varepsilon}\frac{2}{\pi}\left(\frac{d}{D}\right)^2\frac{1}{Re}G-C_{2\varepsilon}\varepsilon\right)$

3.3.2. Characteristics of turbulence

Near of the walls, the relations known as laws of the wall are introduced to connect the values of k and ε to the wall with their values on the first point of adjacent grid to the wall [12]. The values of the turbulent kinetic energy k and the dissipation rate of the turbulent kinetic energy ε are given in the following form:

$$k=\frac{(V_0)^2}{\sqrt{C_\mu}}\left(l_m\frac{\mathrm{d}V_R}{\mathrm{d}y^+}\right)^2 \tag{20}$$

$$\varepsilon=\frac{(V_0)^4}{\sqrt{C_\mu}}(l_m)^2\left(\frac{\mathrm{d}V_R}{\mathrm{d}y^+}\right)^3. \tag{21}$$

Then, the k and ε boundary conditions were deduced while knowing the velocity neighbour to the wall V_R and the distance y of the adjacent node to the solid wall. The necessary stages for this calculation are presented as follows:

- Calculate the product:

$$\frac{\rho V_R}{\mu}y. \tag{22}$$

- Determine the value of y^+ with the interpolation help.
- Determine the rubbing velocity on the wall:

$$V_0=\frac{\mu y^+}{\rho y}. \tag{23}$$

- Calculate the mixing length:

$$l_m=\kappa y^+\left[1-\exp\left(-\frac{y^+}{A}\right)\right]. \tag{24}$$

- Determine:

$$\frac{\mathrm{d}V_R}{\mathrm{d}y^+}=\frac{2}{1+\sqrt{1+4(l_m)^2}}=\frac{2}{1+\sqrt{1+4\left[ky^+\left[1-\exp\left(-\frac{y^+}{A}\right)\right]\right]}}. \tag{25}$$

- Finally, deduct the values of the turbulent kinetic energy k and the dissipation rate of the turbulent kinetic energy ε.

For the flow parallel to the tank wall, the velocity neighbour to the wall V_R is given in the following form:

$$V_R=\sqrt{W_p^2+V_p^2}. \tag{26}$$

In this case, the axial W_p and the tangential V_p velocity compounds are considered:

$$W_p=\frac{W(NR-1,J,K)+W(NR-1,J,K-1)}{2} \tag{27}$$

$$V_p=\frac{V(NR-1,J,K)+V(NR-1,J-1,K)}{2}. \tag{28}$$

On the tank bottom, the same procedure can be used. In this case, the radial U_p and the tangential V_p velocity compounds are considered:

$$V_R=\sqrt{U_p^2+V_p^2} \tag{29}$$

$$U_p=\frac{U(I,J,2)+U(I-1,J,2)}{2} \tag{30}$$

$$V_p=\frac{V(I,J,2)+V(I,J-1,2)}{2}+r(I). \tag{31}$$

At the level of the turbine, the radial U_p and the axial W_p velocity compounds are considered:

$$V_R=\sqrt{U_p^2+W_p^2}. \tag{32}$$

On the blade downstream, the velocity compounds are written as follows:

$$U_p=aU(I,J,K)+(1-a)U(I-1,J,K) \tag{33}$$

$$W_p=bW(I,J,K)+(1-b)W(I,J,K-1). \tag{34}$$

On the blade upstream, the velocity compounds are written as follows:

$$U_p=aU(I,J+1,K)+(1-a)U(I-1,J+1,K) \tag{35}$$

$$W_p=bW(I,J+1,K)+(1-b)W(I,J+1,K-1) \tag{36}$$

with:

$$a=\frac{\Delta R(I-1)}{\Delta R(I)+\Delta R(I-1)} \tag{37}$$

$$b=\frac{\Delta Z(K-1)}{\Delta Z(K)+\Delta Z(K-1)}. \tag{38}$$

3.4. Power consumption

Power consumption is usually used in the design of equipment. Therefore, a detailed knowledge of power of stirred tank configurations is required. The dimensional analysis enables us to characterize power consumption through the power number N_p [17] defined as follows:

$$N_p=\frac{P}{\rho N^3 d^5}. \tag{39}$$

The power P consumed by the turbine in the stirred tanks should be equal to the power dissipated in the liquid. Hence, the power consumption was calculated from the volume integration predicated from the CFD code [17].
In turbulent flow:

$$P_t=\rho\iiint_D\varepsilon\mathrm{d}v. \tag{40}$$

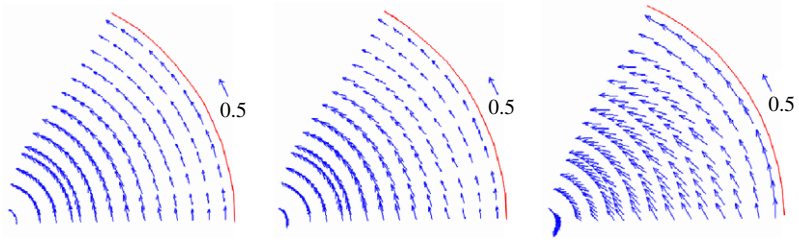

(a) PBT 45°. (b) PBT 60°. (c) PBT 75°.

Fig. 6. Flows patterns induced in r–θ plane define by the axial coordinate $z = 0.3$.

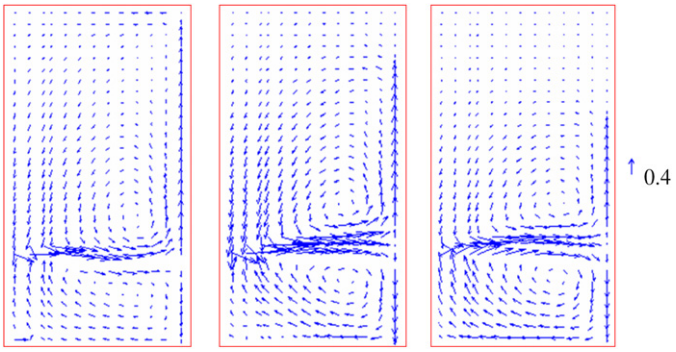

(a) PBT 45°. (b) PBT 60°. (c) PBT 75°.

Fig. 7. Flows patterns induced in r–z plane define by the angular coordinate $\theta = 52°$.

In laminar flow:

$$P_l = \iiint_D \mu \Phi_v \mathrm{d}v. \tag{41}$$

The viscous dissipation rate can be expressed as follows:

$$\Phi_v = \left[2\left[\left(\frac{\partial U}{\partial r}\right)^2 + \left(\frac{\partial V}{r\partial\theta} + \frac{U}{r}\right)^2 + \left(\frac{\partial W}{\partial z}\right)^2\right] + \left[\frac{\partial V}{\partial r} - \frac{V}{r} + \frac{\partial U}{r\partial\theta}\right]^2 + \left[\frac{\partial W}{r\partial\theta} + \frac{\partial V}{\partial z}\right]^2 + \left[\frac{\partial U}{\partial z} + \frac{\partial W}{\partial r}\right]^2\right]. \tag{42}$$

4. Numerical results

The numerical simulations were carried out with our specific CFD code to predict the hydrodynamics results [18]. The entries values were defined by the Reynolds number equal to $Re = 71\,000$ and the Froude number equal to $Fr = 0.19$.

4.1. Flow patterns

Figs. 6 and 7 show a velocity vector plot of the primary flow (U, V) in r–θ plane and the secondary flow (U, W) in r–z plane. The r–θ plane has been defined by the axial coordinate equal to $z = 0.3$. It appeared that the flow was strongly dominated by the tangential component. While comparing these three geometric configurations, it has been noted that the radial component of the velocity vector was weak in the case of the 45° PBT (Fig. 6(a)). For the two other configurations, this component increased (Fig. 6(b) and (c)). The r–z plane has been defined by the angular coordinate equal to $\theta = 52°$. This presentation plane has been situated in the downstream of the blade plane. These figures showed the turbine stream impinging on the outer wall and being deflected in both directions in a wall jet motion producing the upper and lower vortices. Also, it has been clearly noticed that the velocity vector was directly affected by the turbine type. In fact, within the 75° PBT the radial flow was very important. This flow became more and more weak with the reduction of the inclined angle (Fig. 7). Within the 45° PBT, the axial flow was very important near the wall and reaches the top of the liquid surface. This result has been explained by the turbine type allowing a high axial flow. However, within the 60° PBT and the 75° PBT the axial flow has been less intense in top of the stirred tank, which appears a zone of a very weak field. Also, the axial movement generated two zones of recirculation on all sides of these turbines. The zone shapes has been depending from the inclined angle used; the 75° PBT zones showed up a clear symmetry. However, with the feeble angle we noticed that the lower zone expanded mainly in the 45° PBT. Also, the recirculation center zone extended to the inner tank wall while the inclined angle increased, within $r = 0.6$ for the 45° PBT and $r = 0.7$ for the 75° PBT.

4.2. Distribution of turbulent kinetic energy

Figs. 8 and 9 present the evolution of the distribution of the turbulent kinetic energy in the case of different inclined angles equals to $\beta = 45°$, $\beta = 60°$ and $\beta = 75°$. The horizontal presentation planes, defined by the axial coordinate equal to $z =$

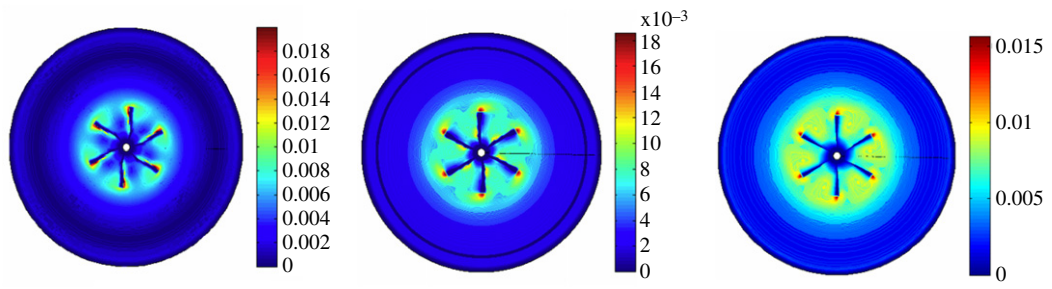

(a) PBT 45°. (b) PBT 60°. (c) PBT 75°.

Fig. 8. Distribution of the turbulent kinetic energy in r–θ plane define by $z = 0.5$.

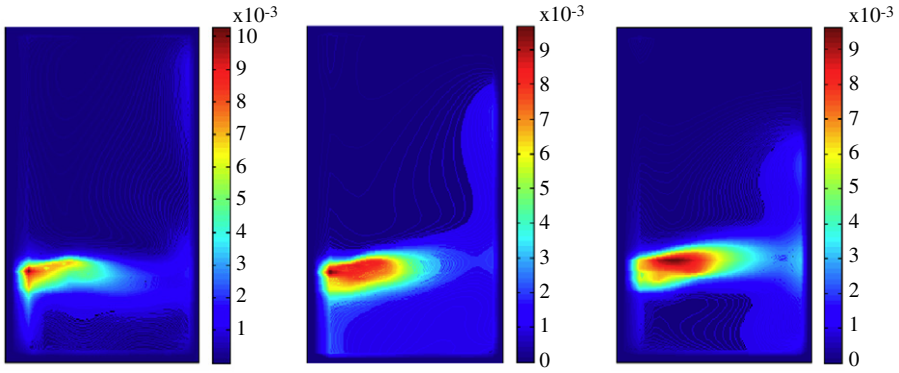

(a) PBT 45°. (b) PBT 60°. (c) PBT 75°.

Fig. 9. Distribution of the turbulent kinetic energy k in r–z plane define by $\theta = 52°$.

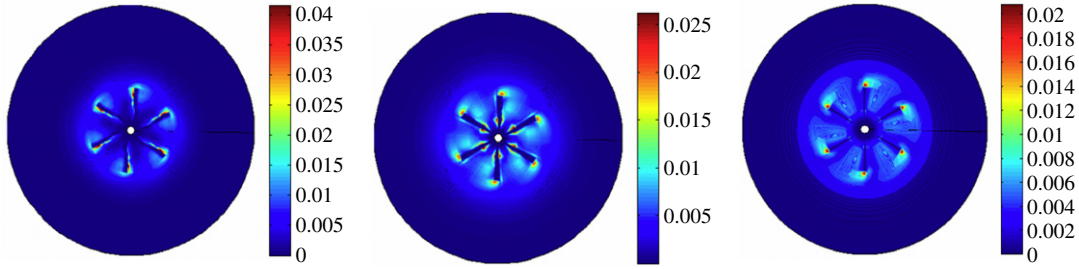

(a) PBT 45°. (b) PBT 60°. (c) PBT 75°.

Fig. 10. Distribution of dissipation rate ε in r–θ plane define by $z = 0.5$.

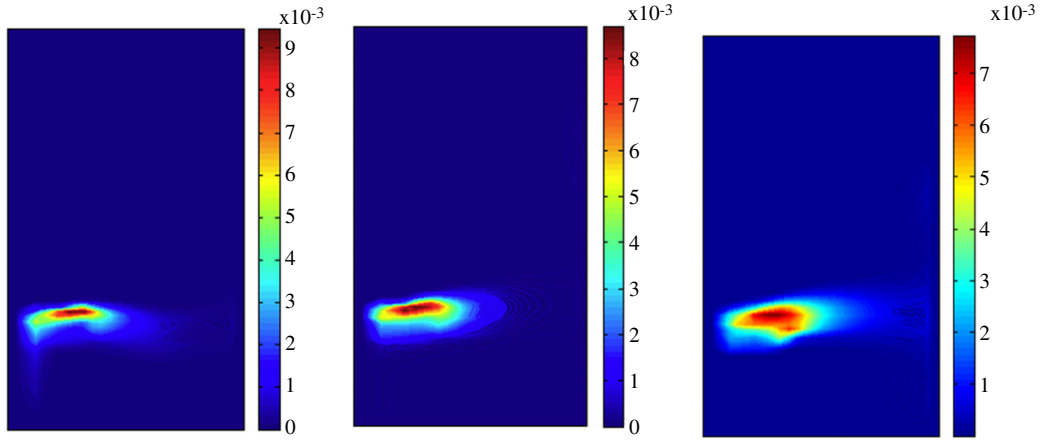

(a) PBT 45°. (b) PBT 60°. (c) PBT 75°.

Fig. 11. Distribution of dissipation rate ε in r–z plane define by $\theta = 52°$.

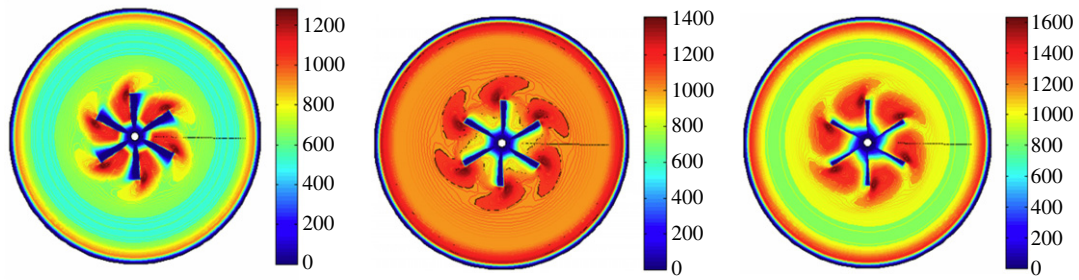

(a) PBT 45°. (b) PBT 60°. (c) PBT 75°.

Fig. 12. Distribution of turbulent viscosity υ_t in r–θ plane define by $z = 0.5$.

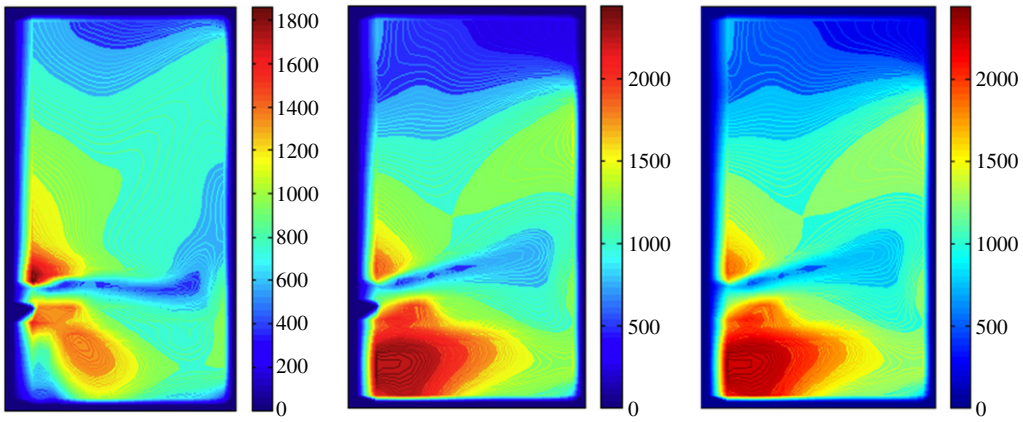

(a) PBT 45°. (b) PBT 60°. (c) PBT 75°.

Fig. 13. Distribution of turbulent viscosity υ_t in r–z plane define by $\theta = 52°$.

0.5, were situated at the mid-height of the turbine. However, the vertical presentation planes were situated in the downstream of the blade plane. They were defined by the angular coordinate equal to $\theta = 52°$. Globally, it has been noted a maximal value in the region localized in the blades tip. In the domain swept by the turbine blades, the turbulent kinetic energy remains enough elevated. Out of this domain, it became quickly very weak. The horizontal presentation planes showed a wake localized in the domain swept by the turbine. This wake has been characterized by the elevated values of the turbulent kinetic energy. While moving away of this domain, these values decreased quickly. The turbine type was then responsible in the characterization of the wake shape. Indeed, according to these results the wake was developed with the increase of the inclined angle β. The wake took the oval shape within a 75° PBT. It shrunk further with the reduction of the inclined angle β. In the vertical presentation planes, the area sites of the maximum values were located in the wake which developed on the upstream of blades.

4.3. Distribution of dissipation rate of the turbulent kinetic energy

Figs. 10 and 11 present the distribution of dissipation rate of the turbulent kinetic energy ε. For the presentation of its features, the same planes adopted in the previous paragraph to study the turbulent kinetic energy were chosen. Therefore, results had shown a huge similarity of the dissipation rate with the turbulent kinetic energy. Indeed, it has been noted that the range of the maximum values of the dissipation rate of the turbulent kinetic energy ε were located in the wake which develops nearly to the blades ends. Mean while, the wake extended more and more with the augmentation of the inclined angle. This result was presented at the Fig. 15, which the power number (integration of the dissipation rate of the turbulent kinetic energy ε) decreased with the decrease of the inclined angle β.

4.4. Distribution of turbulent viscosity

Figs. 12 and 13 present the evolution of the turbulent viscosity distribution in the same planes adopted in the previous paragraphs. The turbulent viscosity has remained rather high in the field swept by blades of the turbine. Very near to the walls and around the turbine, the turbulent viscosity has made a very fast fall. By comparing the three configurations between them, it has been noted that the maximal values of the turbulent viscosity increased with the inclined angle. Indeed, within a 75° PBT the turbulent viscosity has been equal to $\upsilon_t = 2000$. Than, for 60° and

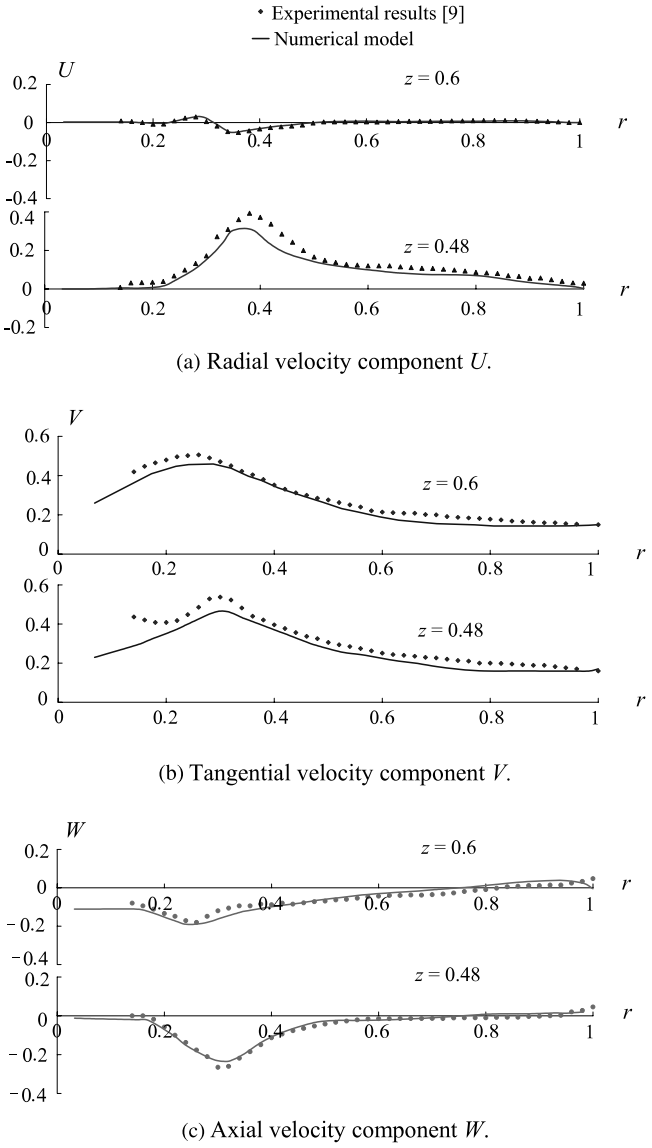

(a) Radial velocity component U.

(b) Tangential velocity component V.

(c) Axial velocity component W.

Fig. 14. Comparison of radial profiles with experimental results ($\theta = 35°$).

45° PBT the turbulent viscosity has been equal to $\upsilon_t = 1500$ and $\upsilon_t = 1400$ respectively. The horizontal presentation plane showed

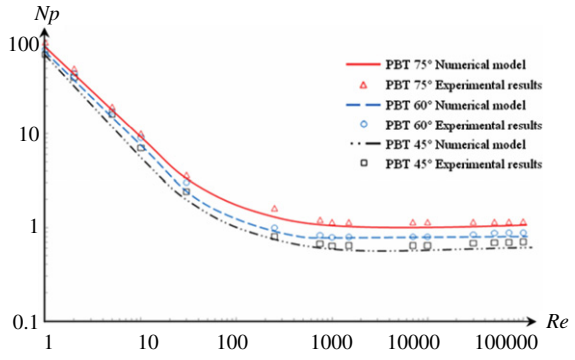

Fig. 15. Power number N_p against Reynolds number Re of pitched-blade turbines.

two wakes localized on all sides of the turbine. These wakes were characterized by the elevated values of the turbulent viscosity. While moving away of this domain, these values decreased progressively until reaching some very weak values near the tank wall. The turbine type has been interfered in the characterization of the wake shape. Within a 75° PBT, the wake form has been developed in the turbine's bottom. However, the wake localized in the turbine's top saved the same form obtained with the 45° PBT.

5. Comparison with experimental results

To verify our computer results, the power number Np were measured and compared with the number calculated from the CFD code as shown in Fig. 15. These results made a strong proof of the inclined angle effects on the power number Np. It appears that the value of the Np decreases as an inclined angle β decreases when compared at the same Reynolds number Re. The downiest value equal to $Np = 0.55$ has been obtained with the 45° PBT. Globally, Np remained constant in the turbulent flow range. But, in the laminar flow range, it is the product $Np\ Re$ which remains constant.

In the other hand, the flow patterns have been compared with ones found by other experimental results [9]. Fig. 14 illustrated the predicted radial profiles of the dimensionless radial, tangential and axial velocity component $U(r)$, $V(r)$ and $W(r)$ within a 45° PBT. These profiles have been defined in the downstream of the blade. The dimensionless axial coordinates has been equal to $z = 0.48$ and $z = 0.6$. These presentation planes were situated respectively in the bottom and in the top of the turbine. This figure adequately portrayed the swirling jets character. In these comparisons, the average error between the experimental results and the numerical results is equal to 7%. The good agreement confirmed the validity of the computer method.

6. Conclusion

In this paper, computer method has been developed to study the PBT design effects. The CFD predictions compared the inclined angles, which were equal to 45°, 60° and 75°, on the stirred tank flow characteristics. These effects have been clearly observed on the local and global hydrodynamics results. In fact, the influence of the inclined angles on the radial and axial flow has been shown. The effect of the impellers configurations on the value of the turbulent characteristics has also been demonstrated. The shape of wake behind the impeller varies with the increase of the inclined angle; it extends more and more with the augmentation of the inclined angle. Furthermore, the values of the power number decreases as an inclined angle decreases when compared at the same Reynolds number. In the future, we propose to develop our CFD code to investigate thermal simulations in complex geometrical configurations.

References

[1] S. Nagata, Mixing: Principles and Applications, John Wiley & Sons: Halstead press, Japan, 1975.
[2] Davide Pirrò, Maurizio Quadrio, Direct numerical simulation of turbulent Taylor-Couette flow, Eur. J. Mech. B Fluids 27 (2008) 552–566.
[3] G. Pianet, E. Arquis, Simulation of particles in fluid: A two-dimensional benchmark for a cylinder settling in a wall-bounded box, Eur. J. Mech. B Fluids 27 (2008) 309–321.
[4] J. Aubin, D.F. Fletcher, C. Xuereb, Modeling turbulent flow in stirred tanks with CFD: The influence of the modeling approach, turbulence model and numerical scheme, Exp. Thermal Fluid Sci. 28 (2004) 431–445.
[5] E.D. Hollander, J.J. Derksen, H.M.J. Kramer, G.M. Van Rosmalen, H.E.A. Van den Akker, A numerical study on orthokinetic agglomeration in stirred tanks, Powder Technol. 130 (2003) 169–173.
[6] D. Dakshinamoorthy, A.R. Khopkar, J.F. Louvar, V.V. Ranade, CFD simulation of shortstopping runaway reactions in vessels agitated with impellers and jets, J. Loss Prevention Process Ind. 19 (2006) 570–581.
[7] T. Kumaresan, J.B. Joshi, Effect of impeller design on the flow pattern and mixing in stirred tanks, Chem. Eng. J. 115 (2006) 173–193.
[8] D.A. Deglon, C.J. Meyer, CFD modelling of stirred tanks: Numerical considerations, Miner. Eng. 19 (2006) 1059–1068.
[9] P.M. Armenante, L. Changgen, C. Chou, I. Fort, J. Medek, Velocity profiles in a closed, unbaffled vessel: Comparison between experimental LDV data and numerical CFD predictions, Chem. Eng. Sci. 52 (1997) 3483–3492.
[10] H. Kchaou, M. Baccar, M. Mseddi, M.S. Abid, Modélisation numérique de l'écoulement interne turbulent généré par une turbine radiale en cuve agitée, Revue Française de Mécanique 1 (2000) 73–79.
[11] B.E. Launder, D.B. Spalding, The numerical computation of turbulent flows, Comput. Methods Appl. Mech. Engrg. 3 (1974) 269–289.
[12] M. Baccar, M.S. Abid, Simulation numérique des comportements hydrodynamiques et thermiques des échangeurs racleurs opérant en régime turbulent, Int. J. Therm. Sci. 38 (1999) 634–644.
[13] Z. Driss, Contribution in studies of the turbines in an agitated vessel, Ph.D. Thesis, National School of Engineers of Sfax, Sfax University, Tunisia, March 2008.
[14] Z. Driss, H. Kchaou, M. Baccar, M.S. Abid, Numerical investigation of internal laminar flow generated by a retreated-blade paddle and a flat-blade paddle in a vessel tank, Int. J. Eng. Simul. 6 (2005) 10–16.
[15] S.V. Patankar, Numerical heat transfer and fluid flow, in: Series in Computational Methods in Mechanics and Thermal Sciences, Mc Graw Hill, New York, 1980.
[16] J. Douglas, J.E. Gunn, A general formulation of alternating direction implicit methods, Numer. Math. 6 (1964) 428–453.
[17] C. Xuereb, J. Bertrand, 3-D Hydrodynamics in a tank stirred by a double-propeller system and filled with a liquid having evolving rheological properties, Chemical Engineering Science 51 (1996) 1725–1734.
[18] Z. Driss, S. Karray, H. Kchaou, M.S. Abid, Computer simulations of fluid–structure interaction generated by a flat-blade paddle in a vessel tank, Int. Rev. Mech. Eng. 6 (2007) 608–617.